

Preparation of a MnO₂@C@MnO Core-shell Heterojunction as a Highly Efficient Electrocatalyst for the Oxygen Evolution Reaction

Hongjuan Hao^{1,2,3}, Hongbin Pu^{1,3,*}, Dingze Lu², Min Zhou², Qiuping Wang², Jiuxin Wang², Yaoheng Su², Lianbi Li², Mengqi Tian²

¹ Institute of Automation and Information Engineering, Xi'an University of Technology, Xi'an 710048, China

² School of Science, Xi'an Polytechnic University, Xi'an, 710048, China

³ Xi'an Key Laboratory of Power Electronic Devices and High Efficiency Power Conversion, Xi'an 710048, China

*E-mail: puhongbin@xaut.edu.cn

Received: 12 July 2022 / Accepted: 20 August 2022 / Published: 10 September 2022

Manganese-based cocatalyst decoration is an effective strategy for constructing an efficient electrocatalyst for the OER. A novel MnO₂ nanowires@C@MnO nanosheet core-shell heterojunction with a unique interfacial microstructure was successfully constructed in this study. The structure and morphology of the as-prepared one-dimensional MnO₂ nanowires and MnO₂@C_x@MnO electrocatalyst were characterized by X-ray powder diffraction (XRD), scanning electron microscopy (SEM), transmission electron microscopy (TEM), Fourier transform-infrared (FTIR), Raman spectroscopy and X-ray photoelectron spectroscopy (XPS). The results clearly revealed that the MnO₂ nanowires@C@MnO nanosheet core-shell heterojunction was a mixture of one-dimensional MnO₂ nanowires and 2D MnO nanosheets. Electrochemical performance tests showed that the electrochemical activity of the MnO₂@20%C@MnO core-shell heterojunction for the OER was considerably enhanced over those of pristine one-dimensional MnO₂ nanowires, MnO₂@15%C@MnO and MnO₂@30%C@MnO. MnO₂@20%C@MnO had a lower overpotential (520 mV at 10 mA/cm²) and Tafel slope (66 mV/dec) than the one-dimensional MnO₂ nanowires (650 mV at 10 mA/cm² and 133 mV/dec, respectively). Electrochemical analyses showed superior OER performance for MnO₂@20%C@MnO, which was mainly attributed to the introduction of C and the coexistence of MnO₂ nanowires and MnO nanosheets. In addition, the MnO₂ nanowires@C@MnO nanosheet core-shell heterojunction provided abundant transport channels for electrons, ions and electrolyte penetration, accelerating the separation of bubbles at the electrode surface.

Keywords: MnO₂, C, Core-shell heterojunction, OER activity.

1. INTRODUCTION

Increasing energy demand in modern society in recent years has motivated the wide study of renewable and sustainable energy development. As a clean and high-efficient energy carrier, hydrogen is regarded as one of the foremost energy candidates to replace fossil fuels [1-6]. Electrochemical technology is considered to be one of the most promising technologies for large-scale hydrogen production [7,8]. However, the limited efficiency of the water splitting process results in slow kinetics for the oxygen evolution reaction (OER) [9]. Therefore, efficient OER electrocatalysts have been developed to accelerate the reaction kinetics and water splitting process [5,10-15]. Extensive studies have shown IrO₂ and RuO₂ to be the best performing OER electrocatalysts to date. IrO₂ and RuO₂ are widely used, but have limitations of scarcity and high-cost [16-18].

Extensive studies have been performed in the last few years to develop OER electrocatalysts that are cost-effective, nontoxic, efficient, and stable. To this end, various electrode materials have been used as electrocatalysts for water splitting, including conducting perovskites [19-22], carbon-based materials [23,24], chalcogenides [25,26], hybrid composites [27,28], metal oxides [29-32] and transition metal oxides [33,34]. In particular, manganese oxide (MnO₂) remains a very attractive OER candidate due to its eco-friendliness, low cost, nontoxicity, high abundance, high activity/stability and promising OER activity [35]. MnO₂ occurs as various structural phases, including α -MnO₂, β -MnO₂, γ -MnO₂ and λ -MnO₂, among which α -MnO₂ has the best electrical properties and highest OER activity when used as an electrochemical catalyst for water splitting. However, to the best of our knowledge, the effect of the morphology of α -MnO₂ on the OER activity and electrochemical performance has not been thoroughly investigated. Therefore, studies have been performed to synthesize α -MnO₂ with various morphologies, including nanowires [36-38], nanotubes, nanoparticles, nanorods and nanosheets [39]. Among these morphologies, α -MnO₂ nanowires exhibit the highest OER performance. The [MnO₆] octahedral units in α -MnO₂ are regularly arranged into 2×2 channels, providing abundant pathways for ions and exposing numerous active sites [40,41]. However, the inherently metastable morphology and low electrical conductivity of MnO₂ necessitates the use of conductive additives to improve the electrical conductivity of MnO₂ for application as an electrode catalyst [42-46].

Carbon-based materials have been extensively studied as conductive additives because of their tunable surface chemistry, excellent electrical conductivity and corrosion resistance. In general, carbon-based materials have a lower electrochemical activity and higher conductivity and stability than metal oxides. Thus, carbon-based materials can be composited with metal oxide catalysts to enhance their electrocatalytic activity and stability. For instance, C nanorod arrays were loaded on CeO₂ derived from metal organic frameworks to prepare a CeO₂/C composite as a highly efficient OER electrocatalyst [47]. Carbon materials have superior electrical conductivity and oxygen mass transfer properties [48,49].

Therefore, the objective of this study was to hybridize C with Mn metal oxides to form electrocatalysts. Carbon-coated MnO₂ was successfully prepared by a liquid phase method and thermal treatment. XRD analysis showed that C reduced Mn⁺⁴ to Mn⁺². SEM and TEM characterization showed that MnO₂-coated carbon existed both as one-dimensional MnO₂ nanowires and two-dimensional MnO nanosheets, resulting in the formation of MnO₂ nanowires@C@MnO nanosheet (MnO₂@C@MnO) core-shell heterojunctions. This novel structure promoted the OER activity of MnO₂. The carbon content of the catalyst was correlated with the OER activity. The results of electrochemical tests showed that among MnO₂@C@MnO heterojunctions with different C mass ratios, the MnO₂@20%C@MnO core-

shell heterojunction successfully decreased the overpotential and Tafel slope from those of the one-dimensional MnO₂ nanowires (650 mV and 133 mV/dec, respectively) to 520 mV at 10 mA/cm² and 66 mV/dec, respectively. There were two main reasons for the enhanced OER activity of MnO₂@20%C@MnO. First, the excellent OER performance and stability resulted from the high specific surface area and outstanding electrical conductivity of the electrocatalyst. Second, synergy between MnO₂ and carbon enabled C to reduce Mn⁺⁴ to Mn⁺², resulting in MnO₂ nanowires@C@MnO nanosheet core-shell heterojunctions with enhanced OER activity.

2. EXPERIMENTAL

2.1 Materials

All the chemicals used during the experiments were of analytical grade and did not require further purification.

2.2 Synthesis of MnO₂ nanowires

KMnO₄ and NH₄F were added to 150 ml of distilled water using the hydrothermal method; the resulting mixture was magnetically stirred for 30 min, transferred to a 200 ml stainless steel reactor, heated at 160 °C for 24 h, and washed several times with distilled water and an ethanol solution. The obtained product was freeze-dried to yield MnO₂ nanowires.

2.3 Synthesis of the MnO₂ Nanowire@C@MnO Nanosheet Core-shell Heterostructure

MnO₂@C core-shell heterojunctions were prepared by the liquid phase method and thermal treatment. MnO₂ nanowires (0.4 g) were dispersed in 160 ml of distilled water. The resulting solution was alternately stirred and ultrasonicated for 6 h to form a uniform suspension (A). Tris (hydroxymethyl) methyl aminomethane (THAM, 2.85 g) was dissolved in 177.5 ml of deionized water, and 73.5 mL of 0.1 M HCl were added to the resulting solution. Following the complete dissolution of THAM, 0.4 g of dopamine was added to the solution form a uniform suspension (B). Then, solution B was added to solution A, and the resulting mixture was stirred for 30 min. The surface of the MnO₂ nanowires was encased in dopamine hydrochloride (PDA). The obtained product was centrifuged and freeze-dried, followed by several washes with water and alcohol, to yield MnO₂@PDA nanowires. MnO₂@C@MnO was produced by annealing the MnO₂@PDA nanowires in an N₂ flow at 600 °C for 2 h at a heating rate of 2 °C/min. The prepared samples were labelled MnO₂@C_x@MnO, where x denotes the C mass ratio, that is, MnO₂@15%C@MnO, MnO₂@20%C@MnO and MnO₂@30%C@MnO.

2.4 Characterization

The crystal structures and phases of the as-prepared samples were investigated by X-ray diffractometry (XRD) using a Rigaku D/MAX2200 PC (Tokyo, Japan) with Cu K α radiation at a

wavelength $\lambda=0.15418$ nm, an operating voltage of 40 kV and an operating current of 40 mA. The sample morphology was characterized by field emission scanning electron microscopy (FE-SEM, using a Hitachi S-4800 & Hiroba EDX electron microscope). The sample morphology was also characterized using a transmission electron microscope (TEM) operated at 200 kV (JEM 3010, JEOL, Tokyo, Japan). Fourier transform-infrared (FT-IR) spectra of the samples were obtained on a Bruker Vector 22 spectrometer. Raman spectroscopy was performed using a BRUKER RFS 27, and a standalone FT-Raman analyser with a resolution of 0.2 cm^{-1} was used to determine the basic dynamic response of the specimens. A specific surface area analyser (JW-BK100B) was used to evaluate the specific surface area and pore volume and size of the samples. The surface electronic states of the samples were measured by X-ray photoelectron spectroscopy (XPS, Kratos Axis Supra) using, an ultrahigh vacuum VG Scientific Corp MK-II electron spectrometer with a multichannel detector. All the binding energies were corrected using C1s at 284.6 eV as a reference.

2.5 Electrochemical measurements

Electrochemical tests were performed on a CHI660E (CHENHUA) electrochemical workstation. The three-electrode system consisted of an Hg/HgO reference electrode, a Pt wire counter electrode, and the prepared sample as the working electrode. All the electrochemical measurements were performed in a 0.066 M phosphate buffer (pH=7). The potential measured by the Hg/HgO electrode was transformed to the reversible hydrogen electrode (RHE) potential using $E_{\text{RHE}}=E_{\text{Hg/HgO}}+0.098+0.059\text{pH}$. Cyclic voltammogram and linear voltammogram curves were obtained over a range of 0.2 V to 1.3 V. Electrochemical impedance spectroscopy (EIS) was conducted over a range of 10 kHz to 0.01 Hz. The OER activity of the samples was evaluated at least three times for each electrocatalytic experiment to test the experimental reproducibility. Equivalent circuit fitting was performed on the EIS data using ZSimpWin 3.3 software.

The activity of the electrocatalyst was evaluated by applying CV and LSV techniques to determine the slope (mV/dec) and overpotential. Stability tests were conducted long-term chronoamperometry.

3. RESULTS AND DISCUSSION

3.1 XRD, SEM and TEM analysis

The XRD patterns of the synthesized 1D MnO_2 nanowires and $\text{MnO}_2@\text{C}@\text{MnO}$ core-shell heterojunction are shown in Figure 1a. The peaks at 12.85° , 18.35° , 25.74° , 28.94° , 36.63° , 37.75° , 39.11° , 41.18° , 42.08° , 46.79° , 49.88° , 56.33° , 60.36° , 65.38° and 69.66° in the pure MnO_2 spectrum were indexed to the (110), (200), (220), (310), (400), (211), (330), (420), (301), (510), (411), (600), (521), (002) and (541) reflections of the $\alpha\text{-MnO}_2$ phase, respectively, matching well with the standard profile of JCPDS No. 44-0141. The sharp intense diffraction peaks in the spectrum of the MnO_2 nanowires indicated high crystallinity. The XRD patterns of the $\text{MnO}_2@\text{C}@\text{MnO}$ core-shell heterojunction are shown in Figure 1b: the diffraction peaks of the $\alpha\text{-MnO}_2$ phase do not appear in the spectrum of the $\text{MnO}_2@\text{C}@\text{MnO}$ core-shell heterojunction produced after C coating using PDA, indicating that the +4 valence of manganese was reduced. The new diffraction peaks at $2\theta = 34.99^\circ$,

40.65°, 58.82°, 70.53° and 73.91° were indexed to face-centred cubic MnO (JCPDS No.07-0230). This result indicated that the final sample was a mixture of MnO₂ and MnO. The absence of the diffraction peaks of MnO₂ in the spectrum of the MnO₂@C/MnO core-shell heterojunction resulted from the growth of the crystal plane of ultrathin MnO nanoplatelets in a preferential orientation. The absence of clear diffraction peaks for C in the spectrum of the MnO₂@C/MnO core-shell heterojunction resulted from the small quantity and high dispersion of C in the samples. The presence of C was further confirmed by SEM, TEM, HRTEM, Raman shift and XPS analyses. The absence of additional diffraction peaks or other phases indicated the high purity of the one-dimensional MnO₂ nanowires and MnO₂@C/MnO core-shell heterojunction. A schematic of the synthesis process and formation of the MnO₂@C/MnO core-shell heterojunction is shown in Figure 1b. The MnO₂@C/MnO core-shell heterojunction was prepared by the liquid phase method and thermal treatment.

The morphologies of the one-dimensional MnO₂ nanowires and MnO₂@C/MnO core-shell heterojunctions were analysed using SEM. As shown in Figure 1c, MnO₂ consisted of a large number of randomly oriented ultralong nanowires with diameters of approximately 50 nm and lengths ranging between 5 and 20 μm. The one-dimensional MnO₂ nanowires were well-dispersed and entangled into a three-dimensional network, where some nanowires were slightly bent. The ultralong structure and high dispersion of the one-dimensional MnO₂ nanowires resulted in excellent flexibility and mechanical stability that could be exploited for chemical separation. Figure 1d shows the corresponding SEM images of the MnO₂@C/MnO core-shell heterojunction. The morphology of the carbon-coated MnO₂@C/MnO core-shell heterojunction was similar to that of the MnO₂ nanowires, showing that the carbon coating did not affect the micromorphology of the MnO₂@C/MnO core-shell heterojunction. However, the diameter of the MnO₂@C/MnO core-shell heterojunction increased, and MnO nanoplates grew on the surface of the MnO₂@C nanowires. The carbon coating stabilized the framework structure and strengthened the electronic conductor. The MnO nanosheets also provided a large number of reaction sites and large specific surface area, promoting the efficient separation and transfer of electrons and holes and the OER performance.

Transmission electron microscopy (TEM) and high-performance transmission electron microscopy (HRTEM) images of the MnO₂@C/MnO core-shell heterojunction are shown in Figure 1e and f for further analysis of the material microstructure. The TEM images of the MnO₂@C/MnO core-shell heterojunction presented in Figure 1e show that the carbon coating did not destroy the nanostructure of MnO₂@C nanowires. MnO₂ nanowires with porous structures formed mainly due to the reduction of manganese dioxide during the carbonization process. An ultrathin C coating could clearly be observed on the surface of the MnO₂ nanowires. MnO₂@C/MnO exhibited an ideal core-shell heterostructure, in which the MnO nanosheets grew on the surface of the MnO₂@C nanowires. The core-shell structure composed of nanowires (one-dimensional) and nanosheets (two-dimensional) facilitated the transfer and separation of electrons and holes and electrochemical reactions [50]. Figure 1f shows a HRTEM image of the MnO₂@C/MnO core-shell heterojunction. The lattice fringes of MnO₂ and MnO can be clearly seen, where the lattice spacings of 0.30 nm and 0.22 nm correspond to the (310) and (200) crystal planes, respectively, which is consistent with the XRD results.

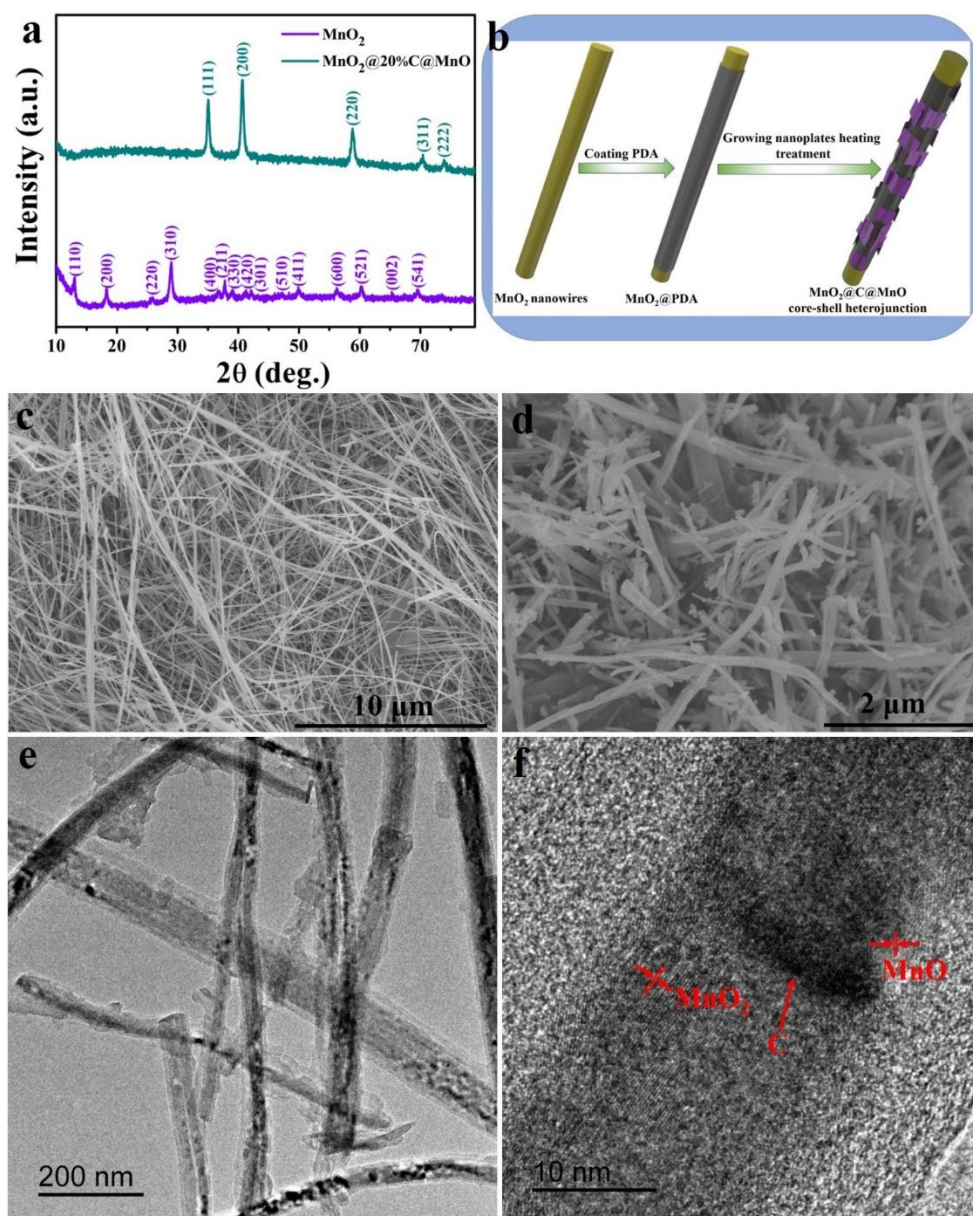


Figure 1. XRD patterns (a) of one-dimensional MnO₂ nanowires and MnO₂@20%C@MnO core-shell heterojunction; The preparation diagram of MnO₂@C@MnO core-shell heterojunction (b); SEM images of one-dimensional MnO₂ nanowires (c) and MnO₂@20%C@MnO core-shell heterojunction (d); TEM images (e) and HRTEM images(f) of MnO₂@20%C@MnO core-shell heterojunction.

3.2 FT-IR and Raman spectra analysis

Figure 2a shows the FT-IR spectra that were obtained to investigate the surface functional groups of the as-synthesized samples. The spectrum of the pure one-dimensional MnO₂ nanowires exhibited the two main characteristic peaks of the Mn-O stretching vibration in the MnO₆ octahedral framework over the 800 to 400 cm⁻¹ range [51,52]. The peak at 1630 cm⁻¹ and the strong and broad peak at 3430 cm⁻¹, corresponded to the stretching vibration of the O-H bond in the adsorbed water during the compression of the sample and KBr, respectively. The intensity of the characteristic peak in the 400-800 cm⁻¹ range

of the FT-IR spectrum of the MnO₂ nanowires was reduced in the FT-IR spectrum of the MnO₂@C@MnO core-shell heterojunction because the introduction of C into the material increased the number of defects, inducing an internal stress that distorted the lattice.

The Raman spectra of the one-dimensional MnO₂ nanowire and MnO₂@C@MnO core-shell heterojunction are shown in Figure 2b. The three characteristic Raman peaks in the spectrum of the one-dimensional MnO₂ nanowire at 386, 576 and 624 cm⁻¹ correspond to Mn-O bonds, that is, the bending vibration of Mn-O-Mn, ν₃(Mn-O) stretching vibration of n₃(Mn-O) caused by Mn⁴⁺ at the bottom surface and symmetric telescopic vibration of ν₃(Mn-O) in the [MnO₆] octahedron, respectively [53]. Compared to the Raman spectrum of the MnO₂ nanowires, the characteristic peaks in the 550-700 cm⁻¹ range were reduced in intensity in the Raman spectrum of the MnO₂@C@MnO core-shell heterojunction, where the characteristic peak at 576 cm⁻¹ was redshifted and the characteristic peak of 624 cm⁻¹ was blueshifted because the introduction of C into the material increased the number of defects, inducing an internal stress that distorted the lattice. The peak in the 550-700 cm⁻¹ range of the Raman spectrum of the MnO₂@C@MnO core-shell heterojunction was wider than that in the Raman spectrum of MnO₂, because the introduction of C created a large number of metal vacancies that destroyed the symmetry of the crystal structure and the compression or stretching of the lattice generated a residual stress. Two other Raman bands appeared at 1347 cm⁻¹ (D band) and 1595 cm⁻¹ (G band) in the spectrum of the MnO₂@C@MnO core-shell heterojunction. The D band was a defect band, and the G band corresponded to the E_{2g} mode (graphitic carbon), indicating that C had been successfully loaded onto the MnO₂ nanowire surface.

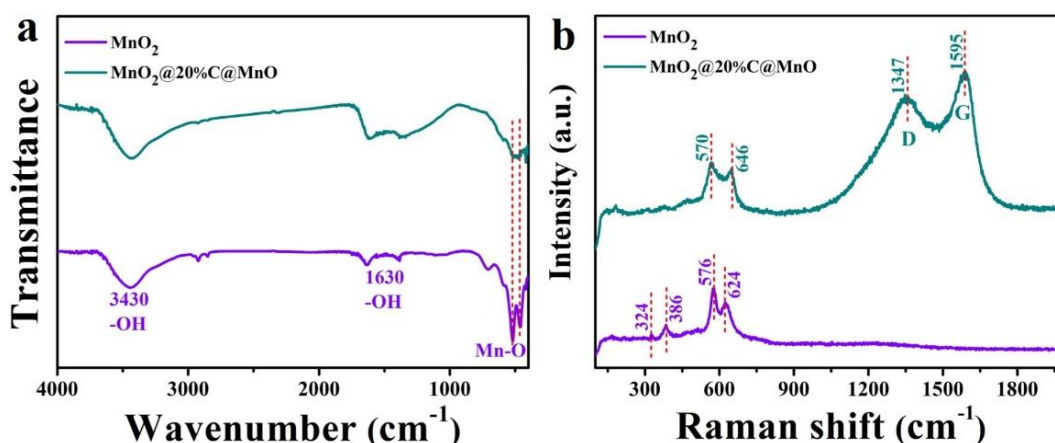


Figure 2. FTIR spectra (a) and Raman spectra (b) of one-dimensional MnO₂ nanowires and MnO₂@20%C@MnO core-shell heterojunction.

3.3 N₂ adsorption-desorption isotherms and pore diameter distribution

As shown in Figure 3, the N₂ adsorption-desorption isotherms of the one-dimensional MnO₂ nanowires and MnO₂@20%C@MnO core-shell heterojunction contained a Type H3 hysteresis loop. MnO₂@20%C@MnO possessed a larger BET specific surface area (Figure 3b, 44.538 m²/g) than the one-dimensional MnO₂ nanowires (Figure 3a, 35.504 m²/g). This high specific surface area facilitated O₂ transport adsorption/desorption, exposed more accessible active sites for the OER, and increased the

catalytic capacity. The high specific surface area also provided sufficient space for the OER to occur, thereby enhancing the electrocatalytic activity of $\text{MnO}_2@20\%\text{C}@MnO$. The reduction of manganese dioxide in the one-dimensional nanowires during carbonization resulted in pore formation in the $\text{MnO}_2@20\%\text{C}@MnO$ core-shell heterojunction. The pore size of $\text{MnO}_2@20\%\text{C}@MnO$ was 22.064 nm (Figure 3b), whereas that of the one-dimensional MnO_2 nanowires was 29.734 nm (Figure 3a). The specific surface area of the $\text{MnO}_2@20\%\text{C}@MnO$ core-shell heterojunction resulted in superior conductivity that facilitated electron transport.

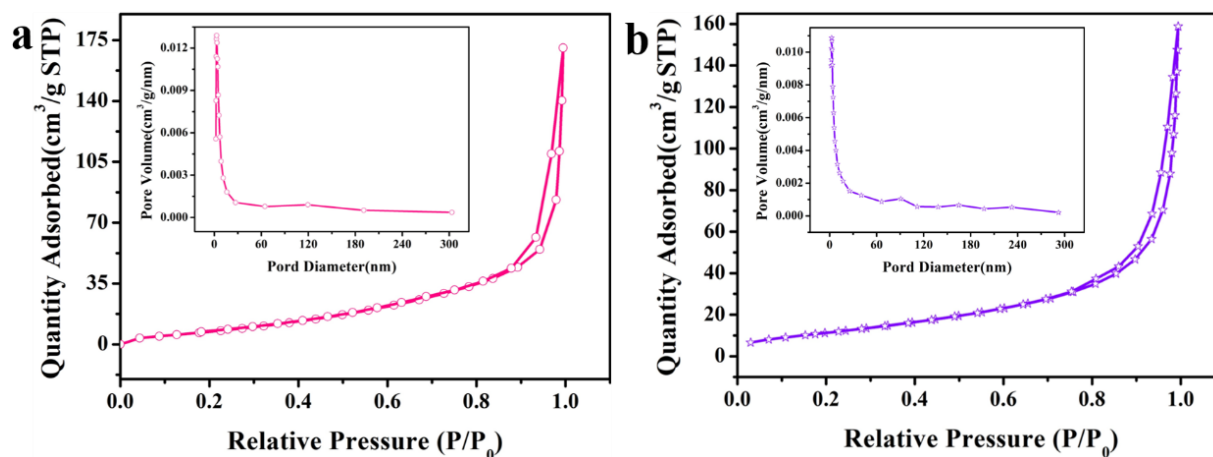


Figure 3. N_2 adsorption-desorption isotherms and pore diameter distribution (insert) of one-dimensional MnO_2 nanowires (a) and $\text{MnO}_2@20\%\text{C}@MnO$ core-shell heterojunction (b).

3.4 XPS analysis

The chemical composition and state of the sample were further determined from the XPS spectra: peaks for C, O and Mn can be seen in Figure 4a. There are no discernible peaks of other impurities in Figure 4a, which is consistent with the XRD analysis. Four core-level signals of C 1s appeared at 292.6 eV, 288.4 eV, 285.8 eV and 284.8 eV corresponding to O=C-O, C=O, C-O and C=C/C=C bands, respectively (Figure 4b). As shown in Figure 4c, the O 1s spectrum contained two main characteristic peaks, corresponding to Mn-O-H (531.2 eV) and Mn-O-Mn (529.9 eV) [54,55]. The peaks in the Mn 2p XPS spectra at ~642.2 eV and 653.2 eV were assigned to Mn 2p_{1/2} and Mn 2p_{3/2}, respectively (Figure 4d). The C-O and Mn-OH bonds were easily to etherified, which promoted the C-O-Mn band transition and made the $\text{MnO}_2@C@MnO$ core-shell heterojunction more robust. The low binding energy of $\text{MnO}_2@20\%\text{C}@MnO$ reflected the migration of electron clouds in the material.

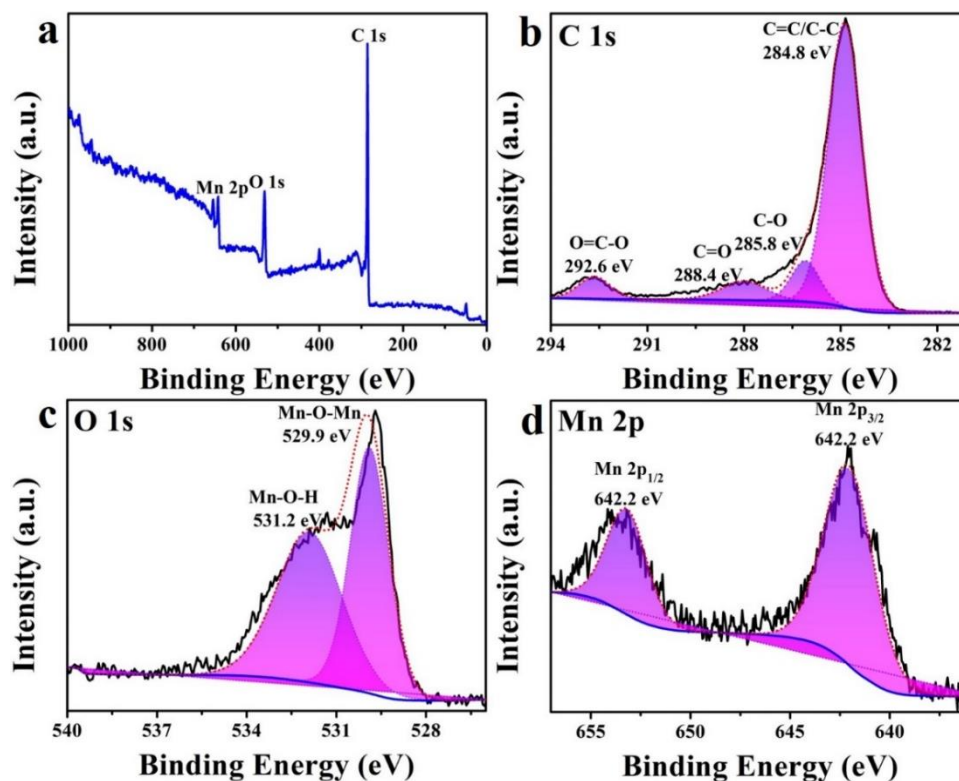


Figure 4. XPS survey spectrum of $\text{MnO}_2@20\%\text{C}@MnO$ (a); C 1s, O 1s and Mn 2p XPS spectra(b-c).

3.5 Electrochemical measurements: OER studies

Figure 5a shows the polarization curves obtained for the 1D MnO_2 nanowires and $\text{MnO}_2@C_x@MnO$ at a scan rate of 50 mV/s. At a current density of 10 mA/cm², $\text{MnO}_2@20\%\text{C}@MnO$ required an overpotential of only 520 mV, which was considerably smaller than that of $\text{MnO}_2@15\%\text{C}@MnO$ (620 mV), $\text{MnO}_2@30\%\text{C}@MnO$ (560 mV) and the MnO_2 nanowires (650 mV). The Tafel slopes of these catalysts reflected the reaction kinetics of the oxygen evolution process. As shown in Figure 5b, the Tafel slope of $\text{MnO}_2@20\%\text{C}@MnO$ was 66 mV/dec, which was superior to that of $\text{MnO}_2@15\%\text{C}@MnO$ (100 mV/dec), $\text{MnO}_2@30\%\text{C}@MnO$ (91 mV/dec) and the 1D MnO_2 nanowires (133 mV/dec). These results showed that the fastest OER kinetics were obtained using $\text{MnO}_2@20\%\text{C}@MnO$.

These enhanced kinetics were further verified by the EIS spectrum. The EIS data were analysed using Nyquist plots, and the fitting results for the equivalent circuits shown in Figure 5c. The Nyquist plots of all the prepared samples contained a semicircle in the high-frequency region, the diameter of which reflected the charge transfer in the sample. The $\text{MnO}_2@20\%\text{C}@MnO$ core-shell heterojunction had the smallest charge transfer resistance, indicating a rapid faradaic process. In the inset of Figure 5c, R_s , R_{ct} , R_{OER} , Q_1 and Q_2 denote the electrolyte resistance, charge transfer resistance, oxygen evolution reaction resistance, constant-phase element 1 and constant-phase element 2, respectively. The measurement data are shown in Table 1: $\text{MnO}_2@20\%\text{C}@MnO$ (11.77 K Ω) had a smaller R_{ct} than the one-dimensional MnO_2 nanowires (99.32 K Ω). This result showed that modifying the one-dimensional MnO_2 nanowires with C nanoparticles significantly reduce the charge transfer resistance, resulting in

enhanced electrical conductivity for the $\text{MnO}_2@20\%\text{C}@MnO$ core-shell heterojunction. The R_{OER} of $\text{MnO}_2@20\%\text{C}@MnO$ (129.4 Ω) was lower than that of the one-dimensional MnO_2 nanowires (166.2 Ω). This result provided strong evidence that $\text{MnO}_2@20\%\text{C}@MnO$ enhanced the OER performance. Figure 5d shows the results of a cyclic voltammetry (CV) test performed in a 0.066 M phosphate buffer (pH 7) at a scanning rate of 30 mV/s using a three-electrode setup. It is important to maintain a neutral pH in artificial photosynthetic systems involving multilayer metal oxides and process equipment. Hence, all the electrocatalytic properties of the samples were determined in a neutral pH system. Figure 5d displays the CVs of the one-dimensional MnO_2 nanowires and $\text{MnO}_2@C_x@MnO$ core-shell heterojunctions. The $\text{MnO}_2@20\%\text{C}@MnO$ core-shell heterojunction exhibited a higher current density than the one-dimensional MnO_2 nanowires, $\text{MnO}_2@15\%\text{C}@MnO$ and $\text{MnO}_2@30\%\text{C}@MnO$.

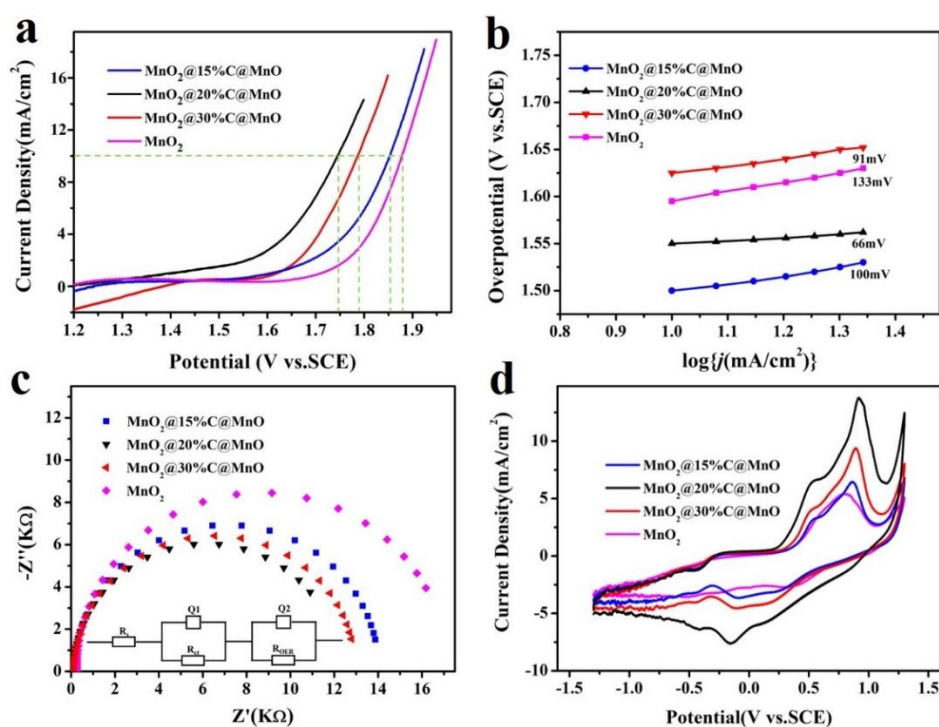


Figure 5. The OER polarization curves in 0.066 M phosphate buffer (pH 7) (a); Tafel plots (b); EIS Nyquist plots (c) and CV curves (d) of the 1D MnO_2 nanowires and different mole ratios of $\text{MnO}_2@C_x@MnO$ core-shell heterojunction.

Table 1. Electrochemical impedance fitting data

| Samples | R_s/Ω | $R_{ct}/K\Omega$ | R_{OER}/Ω |
|---|--------------|------------------|-------------------------|
| MnO_2 | 83.87 | 99.32 | 166.2 |
| $\text{MnO}_2@15\%\text{C}@MnO$ | 82.96 | 40.03 | 146.4 |
| $\text{MnO}_2@20\%\text{C}@MnO$ | 80.33 | 11.77 | 129.4 |
| $\text{MnO}_2@30\%\text{C}@MnO$ | 83.98 | 51.35 | 158.9 |

The double layer capacitance (C_{dl}) was used to evaluate the electrochemically active surface area (ECSA) and inherent electrocatalytic activity of the samples. As shown in Figure 6a,b, the CV curves of

the 1D MnO₂ nanowire and MnO₂@20%C@MnO obtained at scan rates ranging from 20 to 60 mV/s exhibited a rapid current response to voltage reversal at each end potential, reflecting ideal electrochemical capacitive behaviour. Figure 6c shows the C_{dl} values calculated from the CV curves. The higher C_{dl} (6.0 mF/cm²) of the MnO₂@20%C@MnO core-shell heterojunction sample compared to that of the 1D MnO₂ nanowires (3.3 mF/cm²) indicated that the abundant heterostructures, oxygen vacancies and unique porous structures of the nanowires and nanosheets increased the ECSA and created more active sites for the OER. As shown in Figure 6d, the MnO₂@20%C@MnO core-shell heterojunction easily maintained high activity over a long period of 6 h, reflecting the excellent durability of the catalyst.

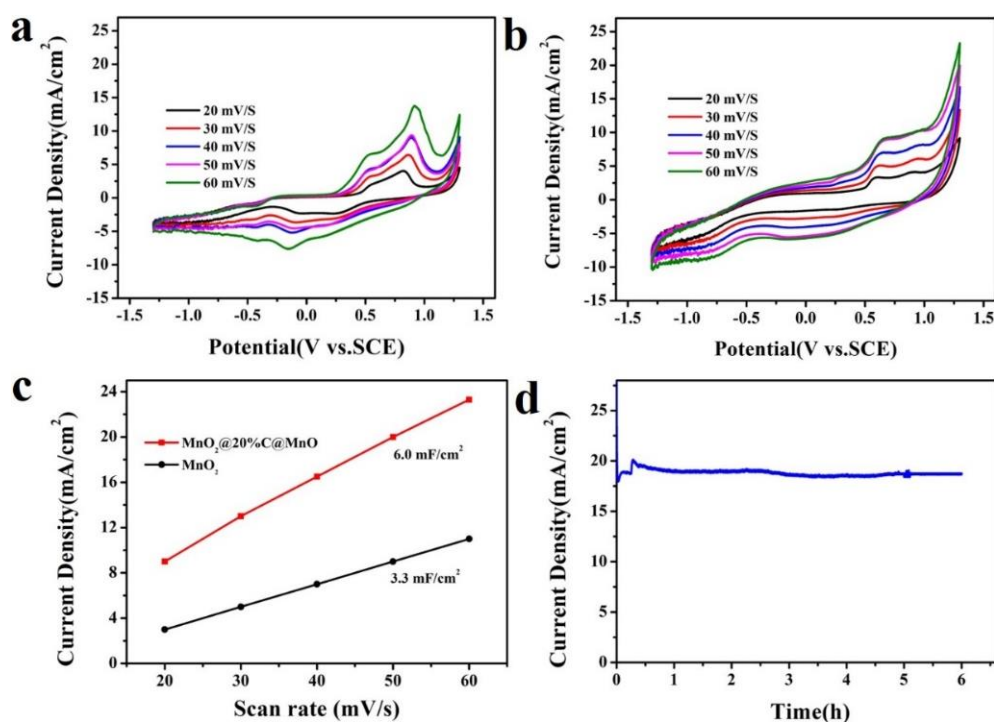


Figure 6. CV curves of the one-dimensional MnO₂ nanowire (a) and MnO₂@20%C@MnO core-shell heterojunction (b) at scan rates of 20, 30, 40, 50 and 60 mV s⁻¹; C_{dl} measurements of the one-dimensional MnO₂ nanowire and MnO₂@20%C@MnO core-shell heterojunction (c); Long-term durability test of the MnO₂@20%C@MnO core-shell heterojunction (d).

To comprehensively evaluate the OER activity of the MnO₂@C@MnO core-shell heterojunction, the OER activities of the MnO₂@C@MnO core-shell heterojunction and MnO_x reported in the literature are compared in Table 2. The overpotential and Tafel slopes of the MnO₂@20%C@MnO core-shell heterojunction were as low as those for MnO_x reported in the literature, such as α -Mn_{0.9}Co_{0.1}O₂ (α -Mn_{0.9}V_{0.1}O₂, α -MnO₂) [56], MnO₂-NS/Cs⁺/NS [57], β -MnO₂ (broken β -MnO₂) [58], α -Mn₂O₃[59], MnO_x NWs[60] and α -MnO₂ (7.6 at% Co and 9.4 at% Ru) [61, 62-68], which was attributed to the good electrical conductivity of the novel core-shell heterojunction. For α -MnO₂-NWN(α -MnO₂-NWS) [69], MnO@rGO [70] and the 1D MnO₂ nanowires (MnO₂@mpg-C₃N₄) [71], the lower overpotential but

higher Tafel slopes compared to those of the MnO₂@20%C@MnO core-shell heterojunction inhibited the OER activity. The comparative analysis presented above shows that the superiority of the MnO₂@20%C@MnO core-shell heterojunction to most MnO_x-based electrocatalysts.

Table 2. OER activities comparisons among MnO₂@C@MnO core-shell heterojunction and previously reported MnO_x in the literatures

| Materials | Overpotential (mV) (at a current density of 10 mA/cm ²) | Tafel Slopes (mV/dec) | Double Layer Capacitance (C _{dl}) (mF/cm ²) | References |
|--|---|-----------------------|---|------------------|
| MnO ₂ | 650 | 133 | 3.3 | This work |
| MnO ₂ @15%C@MnO | 620 | 100 | / | This work |
| MnO₂@20%C@MnO | 520 | 66 | 6.0 | This work |
| MnO ₂ @30%C@MnO | 560 | 91 | / | This work |
| α-Mn _{0.9} Co _{0.1} O ₂ | 690V | 120 | / | [56] |
| α-Mn _{0.9} V _{0.1} O ₂ | 720V | 150 | / | [56] |
| α-MnO ₂ | 740V | 184 | / | [56] |
| MnO ₂ -NS/Cs ⁺ /NS | 613 | 101.3 | / | [57] |
| β-MnO ₂ | 600 | 109.3 | / | [58] |
| Broken β-MnO ₂ | 580 | 101.5 | / | [58] |
| α-Mn ₂ O ₃ | 1740 | 146 | / | [59] |
| MnO _x NWs | 590 | 106 | / | [60] |
| α-MnO ₂ (7.6 at% Co) | 770 | 57 | / | [61] |
| α-MnO ₂ (9.4 at% Ru) | 680 | 62 | / | [61] |
| MnO@Co-N/C | 530 | 112 | / | [62] |
| Nascent δ-MnO ₂ | 590 | / | / | [63] |
| CaMn _x O _y -400/600 | 550 | / | / | [64] |
| MnO | 610 | / | / | [65] |
| Mn ₂ O ₃ | 580 | / | / | [65] |
| Partially oxidized MnO | 530 | / | / | [66] |
| NCs | 550 | / | / | [67] |
| CaMn _x O _y | 550 | / | / | [67] |
| MnO ₂ -NWRs/CNTs350 | 1760 | / | 18.20 | [68] |
| α-MnO ₂ -NWN | 467 | 65.6 | 4.51 | [69] |
| α-MnO ₂ -NWs | 527 | 77.6 | 4.68 | [69] |
| MnO@rGO | 480 | 97 | / | [70] |
| 1D MnO ₂ nanowires | 460 | 105 | / | [71] |
| MnO ₂ @mpg-C ₃ N ₄ | 420 | 90 | / | [71] |

4. CONCLUSIONS

A novel MnO₂ nanowires@C@MnO nanosheet core-shell heterojunction was successfully constructed by the liquid phase method and thermal treatment. During long-term electrocatalysis, the active sites in the MnO₂@C@MnO core-shell heterojunction were fully utilized and the integrity of the active area was maintained. The high specific surface area and mesoporous structure of the MnO₂@C@MnO core-shell heterojunction resulted in efficient electrolyte penetration and fast charge transfer, which enhanced the reaction kinetics. The MnO₂@20%C@MnO core-shell heterojunction exhibited excellent electrochemical performance for the OER. The optimized MnO₂@20%C@MnO had a low overpotential of 520 mV at a current density of 10 mA/cm² and a small Tafel slope of 66 mV/dec. MnO₂@20%C@MnO exhibited moderate stability over 6 h. MnO₂@20%C@MnO exhibited excellent OER activity because the introduction of C and the coexistence of nanowires and nanosheets created a large number of active sites and improved the conductivity.

ACKNOWLEDGEMENTS

This work was financially supported by the Natural Science Foundation of China (Grant No. 51802245, 51677149), Shaanxi Province Innovative Talent Promotion Plan-Young Science and Technology Star (No. 2021KJXX-43), Science and Technology Guidance Project Plan of China National Textile and Apparel Council (No. 2020004), China Postdoctoral Science Foundation Funding (No. 2018M631188), the Shaanxi Provincial Association of Science and Technology Youth Talents Lifting Plan (No. 20180418), Scientific Research Program Funded by Shaanxi Provincial Education Department (No. 18JK0350), the Key Research and Development Program of Shaanxi province (Grant No. 2018ZDXM-GY-003), the Natural Science Basic Research Plan in Shaanxi Province of China (Grant No. 2020JQ-636, 2020JQ-828), the Natural Science Foundation of Shaanxi Province, PR China (Grant No. 2022JM-033) and the Fundamental Research Funds of Shaanxi Key Laboratory of Artificially-Structured Functional Materials and Devices (No. AFMD-KFJJ-21207).

References

1. L. Hammarstrom, *Faraday Discuss.*, 198 (2017) 549.
2. T. Hisatomi and K. Domen, *Faraday Discuss.*, 198 (2017)11.
3. W. Qian, T. Hisatomi, M. Katayama, T. Takata, T. Minegishi, A. Kudo, T. Yamada and K. Domen, *Faraday Discuss.*, 197 (2017) 491.
4. M. M. Najafpour, G. Renger, M. Hołynska, A. N. Moghaddam, E. M. Aro, R. Carpentier, H. Nishihara, J. J. Eaton-Rye, J. R. Shen and S. I. Allakhverdiev, *Chem. Rev.*, 116 (2016) 2886.
5. M. M. Najafpour, F. Rahimi, E. M. Aro, C. H. Lee, S. I. Allakhverdiev, *J. R. Soc. Interface*, 9 (2012) 2383.
6. E. Musazade, R. Voloshin, N. Brady, J. Mondal, S. Atashova, S. K. Zharmukhamedov, I. Huseynova, S. Ramakrishna, M. M. Najafpour and J. R. Shen, *J. Photochem. Photobiol. C Photochem. Rev.*, 35 (2018) 134.
7. S. Anantharaj, S. R. Ede, K. Karthick, S. Sam Sankar, K. Sangeetha, P. E. Karthik and S. Kundu, *Energy Environ. Sci.*, 11 (2018) 744.
8. H. Y. Jin, C. X. Guo, X. Liu, J. L. Liu, A. Vasileff, Y. Jiao, Y. Zheng and S. Z. Qiao, *Chem. Rev.*, 118 (2018) 6337.
9. J. Li, R. Guttinger, R. More, F. Song, W. Wan and G. R. Patzke, *Chem. Soc. Rev.*, 46 (2017) 6124.
10. L. Gong, X. Y. E. Chng, Y. Du, S. Xi and B. S. Yeo, *ACS Catal.*, 8 (2017) 807.

11. C. C. McCrory, S. Jung, J. C. Peters and T. F. Jaramillo, *J. Am. Chem. Soc.*, 135 (2013) 16977.
12. J. Melder, W. L. Kwong, D. Shevela, J. Messinger and P. Kurz, *ChemSusChem*, 10 (2017) 4491.
13. M. M. Najafpour, S. Madadkhani, Z. Zand, M. Hołyńska and S. I. Allakhverdiev, *Int. J. Hydrogen Energy*, 41 (2016) 17826.
14. M. M. Najafpour, S. Salimi, M. Hołyńska and S. I. Allakhverdiev, *Int. J. Hydrogen Energy*, 41 (2016) 4616.
15. G. Elmaci, C. E. Frey, P. Kurz and Z. Karan. *Inorg. Chem.*, 54 (2015) 2734.
16. H. N. Nong, L. Gan, E. Willinger, D. Teschner and P. Strasser, *Chem. Sci.*, 5 (2014) 2955.
17. L. Fu, X. Zeng, C. Huang, P. Cai, G. Cheng and W. Luo, *Inorg. Chem. Front*, 5 (2018) 1121.
18. D. Kang, T. W. Kim, S. R. Kubota, A. C. Cardiel, H. G. Cha and K. S. Choi, *Chem. Rev.*, 115 (2015) 12839.
19. M. Bursell, M. Pirjamali and Y. Kiros, *Electrochim. Acta*, 47 (2002) 1651.
20. J. Suntivich, H.A. Gasteiger, N. Yabuuchi, H. Nakanishi, J. B. Goodenough and Y. Shao-Horn, *Nat. Chem.*, 3 (2011) 546.
21. X. Yang, Y. Liu, S. Li, X. Wei, L. Wang and Y. Chen, *Sci. Rep.*, 2 (2012) 567.
22. X. X. Li, W. Qu, J. J. Zhang and H. J. Wang, *J. Electrochem. Soc.*, 158 (2011) A597.
23. R. Wang, K. Q. Lu, Z. R. Tang and Y. J. Xu, *J. Mater. Chem.*, 5 (2017) 3717.
24. J. Luo, L. Steier, M. K. Son, M. Schreier, M. T. Mayer and M. Gratzel, *Nano. Lett.*, 16 (2016) 1848.
25. J. O. Bockris and T. Otagawa, *J. Electrochem. Soc.*, 131 (1984) 290.
26. J. Suntivich, K. J. May, H. A. Gasteiger, J. B. Goodenough and Y. Shao-Horn, *Science*, 334 (2011) 1383.
27. J. Hu, F. Qian, G. Song, W. Li and L. Wang, *Nanoscale Res. Lett.*, 11 (2016) 469.
28. Z. Ma, G. Shao, Y. Fan, G. Wang, J. Song and D. Shen, *ACS Appl. Mater. Interfaces*, 8 (2016) 9050.
29. A. J. Esswein, M. J. McMurdo, P. N. Ross, A. T. Bell and T. D. Tilley, *J. Phys. Chem. C*, 113 (2009) 15068.
30. Y. Li, P. Hasin and Y. Wu, *Adv. Mater.*, 22 (2010) 1926.
31. Y. Liang, Y. Li, H. Wang, J. Zhou, J. Wang, T. Regier and H. Dai, *Nat. Mater.*, 10 (2011) 780.
32. B. Cui, H. Lin, J. B. Li, X. Li, J. Yang and J. Tao, *Adv. Funct. Mater.*, 18 (2008) 1440.
33. S. Fang, L. Bai, A. Moysiadou, S. Lee, C. Hu, L. Liardet and X. Hu, *J. Am. Chem. Soc.*, 140 (2018) 7748.
34. M. S. Burke, L. J. Enman, A. S. Batchellor, S. Zou and S. W. Boettcher, *Chem. Mater.*, 27 (2015) 7549.
35. M. M. Najafpour, S. Salimi, S. Madadkhani, M. Hołyńska, T. Tomo and S. I. Allakhverdiev, *Photosynth Res.*, 130 (2016) 225.
36. F. Meng, H. Zhong, D. Bao, J. Yan and X. Zhang, *J. Am. Chem. Soc.*, 138 (2016) 10226.
37. S. Lee, G. Nam, J. Sun, J. S. Lee, H. W. Lee, W. Chen, J. Cho and Y. Cui, *Angew. Chem.*, 55 (2016) 8599.
38. P. C. Li, C. C. Hu, T. C. Lee, W. S. Chang and T. H. Wang, *J. Power Sources*, 269 (2014) 88.
39. Y. J. Gu, W. Wen and J. M. Wu, *J. Power Sources*, 469 (2020) 228425.
40. M. M. Najafpour, G. Renger, M. Hołyńska, A. N. Moghaddam, E. M. Aro, R. Carpentier, H. Nishihara, J. J. EatonRye, J. R. Shen and S. I. Allakhverdiev, *Chem. Rev.*, 116 (2016) 2886.
41. X. Wang and Y. Li, *J. Am. Chem. Soc.*, 124 (2002) 2880.
42. Y. Li and H. Dai, *Chem. Soc. Rev.*, 43 (2014) 5257.
43. Z. X. Zhang, Z. F. Li, C. Y. Sun, T. W. Zhang and S. W. Wang, *Catal. Today*, 298 (2017) 241.
44. S. Lee, G. Nam, J. Sun, J. S. Lee, H. W. Lee, W. Chen, J. Cho and Y. Cui, *Angew. Chem.*, 55 (2016) 8599.
45. J. S. Lee, G. S. Park, H. I. Lee, S. T. Kim, R. Cao, M. Liu and J. Cho, *Nano Lett.*, 11 (2011) 5362.
46. Z. Chen, A. Yu, R. Ahmed, H. Wang, H. Li and Z. Chen, *Electrochim. Acta*, 69 (2012) 295.

47. N. Nazar, S. Manzoor, Y. Rehman, I. Bibi, D. Tyagi, A. H. Chughtai, R. S. Gohar, M. Najam-UI-Haq, M. Imran and M. N. Ashiq, *Fuel*, 307 (2022) 121823.
48. D. U. Lee, P. Xu, Z. P. Cano, A. G. Kashkooli, M. G. Park and Z. Chen, *J. Mater. Chem. A*, 4 (2016) 7107.
49. H. Su, X. T. Wang, J. X. Hu, T. Ouyang, K. Xiao and Z. Q. Liu, *J. Mater. Chem. A*, 7 (2019) 22307.
50. Z. Ma, G. Shao, Y. Fan, G. Wang, J. Song and D. Shen, *ACS Appl. Mater. Interfaces*, 8 (2016) 9050.
51. L. Chen, L. J. Sun, F. Luan, Y. Liang, Y. Li and X. X. Liu, *J. Power Sources*, 195 (2010) 3742.
52. L. Lu, H. Tian, J. He and Q. Yang, *J. Phys. Chem. C*, 120 (2016) 23660.
53. C. Julien, M. Massot, R. Baddour-Hadjean, S. Franger, S. Bach, J. P. Pereira-Ramos, *Solid State Ionics*, 159 (2003) 345.
54. F. Larachi, J. Pierre, A. Adnot and A. Bernis, *Appl. Surf. Sci.*, 195 (2002) 236.
55. Q. W. Tang, L. H. Jiang, J. Liu, S. L. Wang and G. Q. Sun, *ACS Catal.*, 4 (2014) 457.
56. J. M. Lee and S. J. Hwang, *J. Solid State Chem.*, 269 (2019) 354.
57. Q. Kang, L. Vernisse, R. C. Remsing, A. C. Thenuwara, S. L. Shumlas, I. G. McKendry, M. L. Klein, E. Borguet, M. J. Zdilla and D. R. Strongin, *J. Am. Chem. Soc.*, 139 (2017) 1863.
58. G. Q. Han, Y. R. Liu, W. H. Hu, B. Dong, X. Li, X. Shang, Y. M. Chai, Y. Q. Liu and C. G. Liu, *J. Electrochem. Soc.*, 163 (2016) H67.
59. M. Jahan, S. Tominaka and J. Henzie, *Dalton Trans.*, 45 (2016) 18494.
60. X. F. Luo, J. Wang, Z. S. Liang, S. Z. Chen, Z. L. Liu and C. W. Xu, *Int. J. Hydrog. Energy*, 42 (2017) 7151.
61. M. Lubke, A. Sumboja, L. McCafferty, C. F. Armer, A. D. Handoko, Y. H. Du, K. McColl, F. Cora, D. Brett, Z. L. Liu and J. A. Darr, *ChemistrySelect*, 3 (2018) 2613.
62. Y. N. Chen, Y. B. Guo, H. J. Cui, Z. J. Xie, X. Zhang, J. P. Wei, Z. Zhou, *J. Mater. Chem. A*, 6 (2018) 9716.
63. Y. F. Li and Z. P. Liu, *J. Am. Chem. Soc.*, 140 (2018) 1783.
64. H. Simchi, K. A. Cooley, J. Ohms, L. Huang, P. Kurz and S. E. Mohny, *Inorg. Chem.*, 57 (2018) 785.
65. K. L. Pickrahn, W. P. Sang, Y. Gorlin, H. B. R. Lee, T. F. Jaramillo and S. F. Bent, *Adv. Energy Mater.*, 2 (2012) 1269.
66. K. Jin, A. Chu, J. Park, D. Jeong, S. E. Jerng, U. Sim, H. Y. Jeong, C. W. Lee, Y. S. Park, K. D. Yang, G. K. Pradhan, D. Kim, N. E. Sung, S. H. Kim and K. T. Nam, *Sci. Rep.*, 5 (2015) 10279.
67. H. Simchi, K. A. Cooley, J. Ohms, L. Huang, P. Kurz and S. E. Mohny, *Inorg. Chem.*, 57(2017) 785.
68. N. N. Xu, J. W. Liu, J. L. Qiao, H. T. Huang and X. D. Zhou, *J. Power Sources*, 455 (2020) 227992.
69. Y. D. Chen, S. J. Yang, H. F. Liu, W. Zhang and R. Cao, *Chinese J. Catal.*, 42 (2021) 1724.
70. G. T. Fu, X. X. Yan, Y. F. Chen, L. Xu, D. M. Sun, J. M. Lee and Y. W. Tang, *Adv. Mater.*, 30 (2018) 1704609.
71. G. Elmacl, A. S. Erturk, M. Sevim and O. Metin, *Int. J. Hydrogen Energy*, 44 (2019) 17995.